Potential megathrust co-seismic slip during the 2020 Sand Point, Alaska strike-slip earthquake

Sean R. Santellanes[1], Diego Melgar[1], Brendan W. Crowell[2], Jiun-Ting Lin[1]

[1]Department of Earth Sciences, University of Oregon

[2]Department of Earth and Space Sciences, University of Washington

Abstract

In October 2020, a Mw 7.6 earthquake struck to the south of the Shumagin Islands in Alaska, nearly 3 months after the Mw 7.8 Simeonof megathrust event. The initial models of the earthquake indicated a largely strike-slip rupture; however, the observed tsunami was much larger and widespread than expected for the focal mechanism. We investigate what sea surface deformation is necessary to recreate the tsunami waveforms using water-level inversion techniques. We find that the sea surface deformation does not resemble that expected from a purely strike-slip earthquake. Instead we propose that it is likely that considerable slip occurred on the megathrust, westward and updip from the previous July event. The Sand Point earthquake potentially released ~2 meters of accumulated slip in the western Shumagin Gap, but likely did not slip updip of ~15 km depth, which still leaves a significant hazard for a shallow tsunamigenic earthquake in the future.

Plain Language Summary

Strike-slip earthquakes often are not a cause for worry when it comes to tsunami hazards. They usually produce negligible amounts of uplift and subsidence on the seafloor. However, a magnitude 7.6 earthquake seemingly did the impossible and caused a hazardous (coastal amplitudes >30 cm) tsunami in Alaska and Hawai'i. We gauge how the earthquake was able to do so by looking at water-level data from tide gauges and open ocean buoys. We find that the strike-slip earthquake had help from a megathrust earthquake in creating the tsunami, and the megathrust earthquake was "silent" in the seismic data.

1. Motivation

Tsunamis are most often the result of earthquake sources at subduction zones. Megathrust co-seismic slip is a key process for tsunamigenesis as it typically produces sea surface deformations large enough to result in hazardous waves (coastal amplitudes > 30cm). The Shumagin segment of the Alaskan Subduction Zone (Figure 1) has been characterized as an area that has largely been devoid of great earthquakes (Mw >= 8.0) for at least the past 100 years (Davies et al, 1981). This may be due to it being in transition between the fully creeping Sanak segment to the west and fully locked Semedi segment to its east (Li & Freymueller, 2018). The Shumagin segment is different with respect to its neighboring segments, great earthquakes have been observed in the Sanak segment (Mw 8.6, 1946) and the Semedi segment (Mw 8.3, 1938) (Davies et al., 1981; Li & Freymueller, 2018; Witter et al., 2014). These have been shown

to have produced large, devastating tsunamis from megathrust co-seismic slip. The last known great earthquake in the Shumagin segment is commonly thought to have occurred in 1788; however, geologic observations point that two large earthquakes occurring in just over a month between each other would be more consistent with those observations (Witter et al., 2014).

On 22 July, 2020, the Mw 7.8 (M_0=6.91x10^{20} N-m) Simeonof earthquake occurred on the megathrust portion near Simeonof Island (FIgure 1, Crowell & Melgar, 2020), producing a small tsunami (Liu et al., 2021; Larson et al., 2021) with ~30cm maximum amplitude at the nearby Sand Point, AK tide gauge (amplitude measured relative from normal sea level). The tsunami had small amplitudes (< 1cm) in the open ocean buoys in the surrounding area. In stark contrast to this, the 19 October, 2020 Mw 7.6 (M_0 = 2.82x10^{20} N-m) Sand Point earthquake produced a tsunami with maximum amplitude of 76 cm at the same Sand Point tide gauge, and a ~0.30 cm maximum amplitude at the Hilo, Hawai'i tide gauge, more than 3800 km away. It was also recorded clearly by 4 open ocean buoys, as seen in Figure 1. The focal mechanism of this earthquake according to the U.S Geological Survey's (USGS) W-Phase solution was a westward-dipping strike-slip fault (Figure 1) with a 71% double-couple component. The shaking reached MMI VII for both events. How the Sand Point event was able to produce a significantly larger tsunami given it is ~2.5 times smaller, by scalar moment, than the Simeonof event and that it has a strike-slip focal mechanism is not clearly understood. It has been generally accepted that strike-slip earthquakes do not produce large enough amounts of vertical sea surface deformation necessary to generate tsunamis with amplitudes > 30 cm in the near-field. The peculiar nature of the Sand Point earthquake's tsunami was highlighted again by the 2021 Mw 8.18 (M_0 = 2.36x10^{21} N-m) Chignik earthquake (Figure 1), another low-angle thrust which also failed to produce a sizable tsunami. It had amplitudes of 15.2 cm at Sand Point. Again, the Sand Point earthquake was a full order of magnitude smaller than Chignik by scalar moment, yet it still has somehow produced the largest tsunami of the three-event sequence.

To unravel what causes co-seismic tsunamis, a common approach is to use finite fault models to derive the deformation of the seafloor and use that as a tsunami initial condition. However, as we will show here, the finite fault model from the National Earthquake Information Center (NEIC) does not reproduce either the timing of arrivals or the amplitudes of the tsunami signals at the Alaskan and Hawaiian tide gauges, or the open ocean buoys (Figure 2). In fact, our findings will argue that no strike-slip earthquake ever could in this region.

We take an alternate approach. We use the tide gauge and open ocean buoy data to solve directly for a sea surface deformation model that is able to recreate the tsunami signals at all sites. This technique is attractive because it is devoid of any assumptions on what causes the deformation and simply solves directly for the required initial condition. We then use this inferred sea-surface deformation to explore what tectonic sources, if any, could produce such an

initial condition. We will show that the sea surface deformation is most consistent with slip on both the strike-slip fault and the neighboring megathrust. The location we propose for the megathrust slip is just updip of the 2020 M7.8 Simeonof earthquake but stops at 15 km depth; it most likely does not extend to the trench. Our findings leave an open question which, while we propose answers to, are not resolved in this work.

2. Data & Methods

2.1 Data & Modeling

The Mw 7.6 Sand Point tsunami was observed by two near-field tide gauges in the Aleutian Islands, two far-field tide gauges on the island of Hawai'i and four Deep-ocean Assessment And Reporting of Tsunamis (DART) buoys (Figure 1) (Titov et al., 2005). We also use vertical deformation measured by one high-rate Global Navigation Satellite System (GNSS) site, AC12 and processed by the University of Nevada Reno (Blewitt et al., 2018). The bulk of our analysis and subsequent inversion methods are anchored around the water-level data while AC12 provides a constraint on the inferred deformation on land for the inversion methods, with ~10 cm of subsidence. The tide gauges utilized in the inversion have a sampling rate of 1 min, and the DART buoys, in event mode, have a sampling rate between 15 sec and 1 min. We de-tide the water-level data of the observations and models with a bandpass filter between 2 min-120 min for the tide gauges and 15 min to 120 min for the DART buoys. Additionally, to correct the far-field travel time error introduced by unmodeled effects from a compressible seafloor (Tsai et al., 2012), we apply a simple cross-correlation to shift the synthetic data at Hilo.

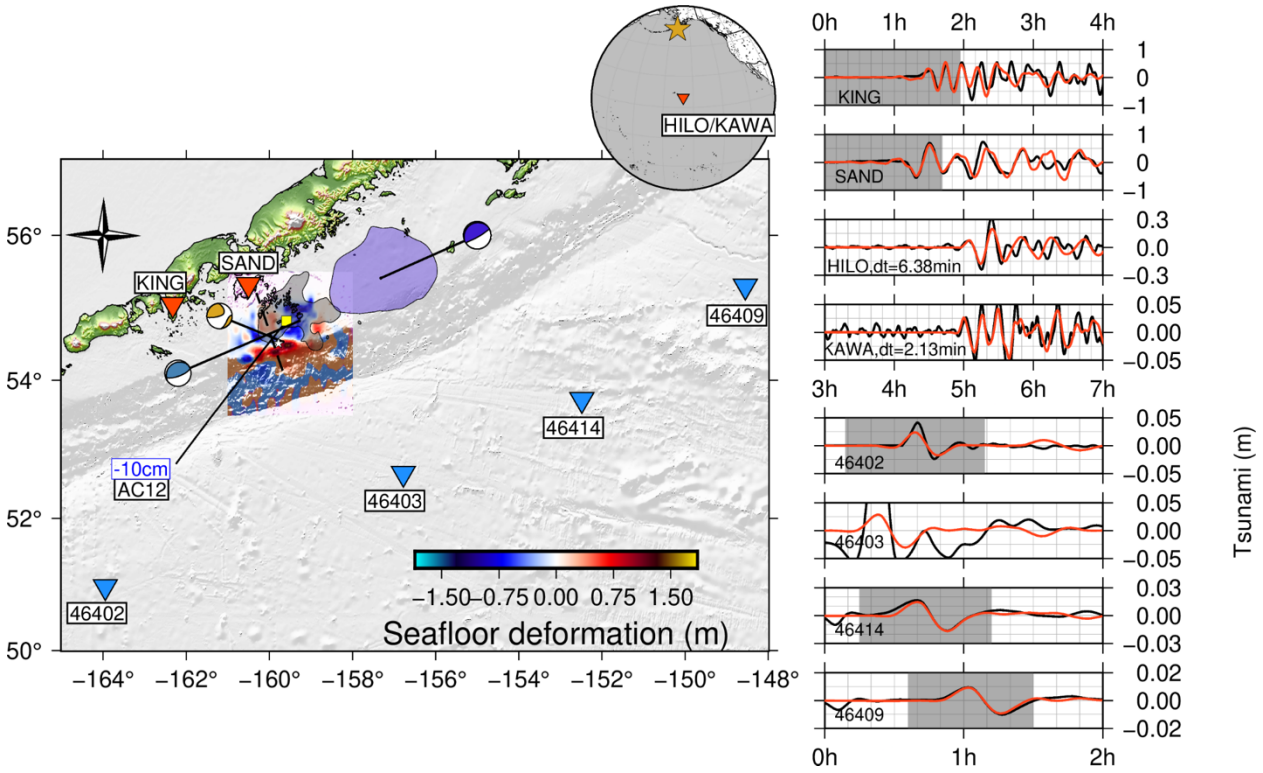

Figure 1. *Final model of the sea surface deformation for the Sand Point earthquake. Red triangles are the tide gauges in Alaska and Hawai'i. Blue triangles are the DART buoys. We plot the sea surface deformation alongside the rupture zones for the M7.8 Simeonof (grey) from Crowell & Melgar, 2020 and M8.2 Chignik (blue) from the USGS. The dashed line is the surface trace for the W-Phase nodal planes used in the USGS finite fault model. The black tsunami waveforms are the 1 min observed data, and the red ones are the simulation results from the sea surface deformation model. Gray boxes outline which portions of the tide gauges and DARTs were used in the tsunami inversion scheme. We shifted the simulated tsunami waveforms for Hilo by 6.38 min and Kawaehai by 2.13 min to match the observed data at the tide gauges.*

For the tsunami Green's functions needed by the inversion, and for subsequent, more detailed modeling, we use the open source GeoClaw code (LeVeque et al., 2011). It solves the non-linear shallow-water equations using adaptive mesh refinement so that areas of high tsunami complexity, such as the case with tide gauge locations, can be refined to higher discretization levels. We use SRTM15 (450m pixels) for the model domain in Figure 1. We also use arcsec (~10 m pixels) bathymetry/topography to provide greater detail for the areas around the tide gauges. The tsunami simulations are run at 4 levels of mesh refinement starting at 5 arcmin (~7.5 km) and ending at 3 arcsecs (~90 m). Output is collected at the locations of the real world tide gauges and DART buoys.

2.2 Elementary Gaussian Tsunami Source Inversion

In order to estimate the tsunami source, we follow the method generally described by Tsushima et al. (2009) and as implemented by Lin et al. (2020). We compute the Green's functions for unit source areas surrounding the strike-slip rupture from the USGS finite fault model (Figure 1). Again, with this method, we side-step any complexities of the tsunami source that may arise due to complex fault geometry, multi-fault ruptures, or other tsunami sources such as landslides. The Green's functions are calculated for a 2-D Gaussian tsunami source with the standard deviation of 5 km and amplitude of 1 m. The spacing between the center of the tsunami sources is 10 km. The Gaussian nature of the tsunami source elements ensures that they overlap at the margins, so that smooth variations of sea surface displacements can be expressed with a discrete sum of sources. We use a total of 428 sources in the inversion. We regularize the inversion by a Tikhonov operator of zeroth order and then employ a L-curve criterion from the inversions to find the right level of trade-off between smoothing and misfits of the inversion (Figure S1). The distribution of the tsunami source elements is shown in Figure S2. Green's functions for the two Alaskan tide gauges and four DART buoys were computed for each tsunami source. They were later used for inversion and forward modeling of the tsunami. DART buoy data is produced by a bottom pressure recorder. Seismic arrivals, such as Rayleigh waves and acoustic phases, introduce pressure signals which do not reflect tsunami energy. As a result it is important to mask out these spurious signals and use only the portions that reflect the tsunami itself. At DART station 46403 the tsunami's arrival occurred while seismic signals were still visible and could not be used in the inversion. For the tide gauges it has been shown that only the first ~1-1.5 wavelengths can be reliably inverted with later arrivals being difficult to account for in linear inversions (Melgar & Bock, 2013; Yue et al., 2015); as a result we used only the first arriving signals in the inversion. Figure 1 shows as shaded regions which time intervals of the water-level data were used in the inversion. The sea surface deformation model was denoised by the method described in Text S1.

2.3 Ensemble Modeling of Strike-Slip ruptures

Figure 2 shows the results of forward modeling of the tsunami with the USGS finite fault as initial condition. It does not reproduce any of the tsunami waveforms in the near- or far-field. Teleseismic finite fault inversions have been used successfully in many studies of large (Mw7+) earthquakes (e.g. Ye et al., 2015, Hayes, 2017). However, since they do not include regional observations, they can have limited spatial resolution. Thus, it is possible that the Sand Point tsunami was indeed produced by a strike-slip earthquake albeit one with a significantly different slip distribution than what was imaged by teleseismic data. To explore whether it is possible that a strike-slip event with a different slip distribution explains the tsunami, we generated 40 stochastic slip distributions in the Mw7.6-Mw7.7 magnitude range. We used the FakeQuakes approach described by Melgar et al. (2016) and produced the rupture models on the same

faulting geometry as used by the USGS finite fault. The resulting ruptures are in (Supplementary Figure S3 and S4). For each rupture, we modeled the tsunami propagation to the Alaska and Hawaii tide gauges and to the DART buoys.

2.4 Slip Inversion of the Vertical Deformation Field

Finally, to test whether the vertical deformation field required by the water level data can be attributed to coseismic slip, we perform a static slip inversion. We use the MudPy suite of codes (Melgar & Bock, 2015) and simultaneously invert on the same strike-slip fault geometry as the USGS finite fault but we also add the megathrust geometry used by Crowell & Melgar (2020) for the Simeonof earthquake, which has a fault extent that easily exceeds the limits of the Sand Point rupture. The inversion is regularized using a zeroth order Tikhonov approach and the optimal regularization parameter is obtained from the L-curve criterion. We resample the vertical seafloor deformation into 3663 points which are equally weighted in the inversion.

3. Results & Discussion

3.1 Sea surface deformation model

Our final preferred sea surface deformation model is shown in Figure 1. The model has 0.11m of subsidence at AC12, compared to 0.10m in the observed data. It has a maximum uplift of 1.41 m and maximum subsidence of 1.19 m, which is located primarily in the area roughly coincident with the surface projection of the NEIC finite fault model. The deformation pattern is visibly not consistent with a strike-slip fault as it is mostly oriented in the trench-parallel direction. As a comparison, Figure 2 shows the expected pattern from the USGS model and fits to the water-level data using it as an initial condition, the expected deformation is much smaller with peak subsidence of 0.23 m and peak uplift of 0.39 m. The arrivals are ~1 hr too early at local tide gauges and too small at all sites in the near- and far-field. The extended trench parallel deformation and uplift/subsidence pattern in the water-level inversion is more akin to what is expected of a traditional megathrust rupture. We use the uplift/subsidence pattern derived from only the first ~1-1.5 wavelengths of water-level data (Figure 1) for a fully non-linear propagation model run for 7 hrs of propagation time. The tsunami waveform misfits are generally small, see Table S1 for RMSE. The nullspace shuttle result lowers the RMSE most notably at the Sand Point tide gauge, and it reduces the errant first arrival from noise from the full model (see Figure S5). The model is able to capture the timing of the waveforms well and is able to match the general shapes. We conducted a checkerboard test and find that while there is some unavoidable smearing resolution is similar everywhere in the inversion domain (Figures S6-8)

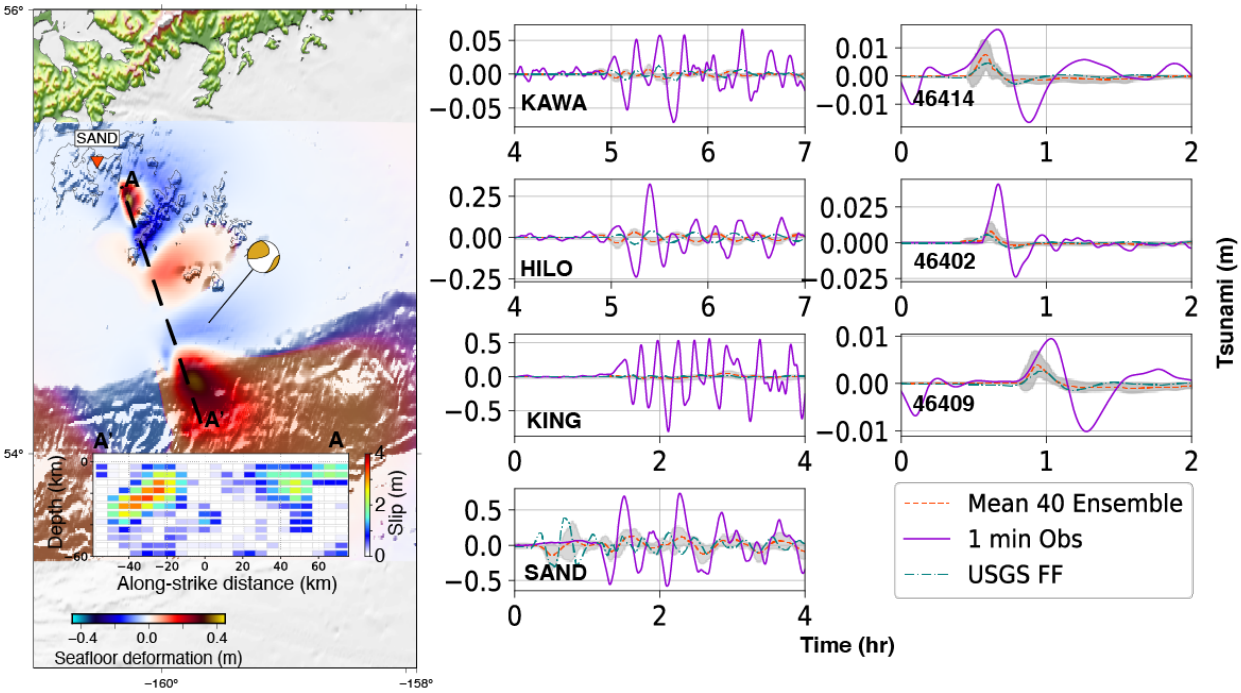

Figure 2. *The USGS finite fault model and tsunami models. (A) The predicted vertical deformation from the USGS model is shown. The dashed line labeled A-A' is the surface projection of the fault. (B) Tsunami waveforms using the USGS model and the stochastic slip as initial conditions. The USGS solution is shown as the dash-dot teal line, the 40 member stochastic slip ensemble mean is shown in orange dashed line , and the 1 min observations are shown in magenta. The gray area around the ensemble shows 2 standard deviations from the mean. The bounds on seafloor deformation are different compared to the other plots to allow for ease of viewing the strike-slip deformation.*

3.2 Can the uplift pattern be consistent with strike-slip faulting?

Teleseismic moment tensors are clear that strike-slip faulting is the predominant mechanism for the seismic data, although the NEIC W-phase moment tensor shows a significant (29%) non double-couple component. We explore in more detail whether a strike-slip faulting mechanism, subject to some modifications, can be made parsimonious with the tsunami observations. Recent research has shown that given the right conditions a strike-slip rupture can produce larger than expected tsunamis (Elbanna et al, 2021). However, this requires a special configuration of the coastline and earthquake which is not present here. The 40-member ensemble of strike-slip ruptures based off of the NEIC finite fault solution, shows that the strike-slip mechanism based on those geometries cannot reproduce any of the features of the tsunami waveforms at any of the near- and far-field tide gauges or DART buoys. Perhaps the most glaring issue for the

strike-slip solution is that the stochastic models systematically lack the ability to reproduce any of the basic features of the tsunami waveforms at the King Cove and Hawaiian tide gauges. Upon visual inspection of Figure 2, it is evident that the sea surface deformation produced by these rupture scenarios is insufficient. In both the 40-member ensemble and the NEIC solution, the tsunami arrives ~1 hour too early and has too low a maximum amplitude (trough-to-crest) at ~0.4m compared to the actual 1.32 m at the Sand Point tide gauge, the tide gauge where the ensemble and NEIC solution do better for the waveform. These findings strongly suggest that a strike-slip earthquake by itself is insufficient to reproduce the tsunami waveforms. Some other phenomenon must be happening concurrently.

The other alternative that can be considered is the possibility of an underwater landslide or slump. Given the resolution of the tsunami sources for the elementary Gaussian inversion, we would not be able to resolve deformations caused by localized failures. We cannot rule out the possibility of one occurring with the inversion scheme employed by this study. However, a simple thought experiment argues against it being a significant source. It has been shown that landslides have a distinct dipole behavior, and given their usual source sizes, attenuate quickly with distance. They are seldom seen in the far-field, compared to the seismic sources, provided they have the same energy (Okal & Synolakis 2003). The tsunami waveforms at the Hawaiian tide gauges, ~3800km away, showed that considerable energy was able to traverse the distances between the source in the Shumagin segment and Hawaii. This would be uncharacteristic of a landslide source. In order for this to be a viable mechanism, there would need to be higher tsunami amplitudes in the near-field at the Alaskan tide gauges, which are not observed. Another issue against this potential source is where the sea surface deformation is relative to the trench. A landslide source would need to occur on areas with steep slopes; however, the sea surface deformation preferred by the model is located on a relatively flat area of the continental shelf (Bécel et al., 2017). If slumps were occurring on the prism, there would be some attempt by the inversion scheme to place deformations there.

3.3 Megathrust Co-seismic Slip and Implications

We are left to conclude that the most likely type of source to explain the tsunami is slip along the megathrust. When we use the vertical deformation model from Figure 1 in a joint static slip inversion on the strike-slip fault and the megathrust we obtain the slip distribution seen in Figure 3. We observe from Figure 1 that the sea surface deformation pattern is more consistent with that of thrust faulting rather than other modes of rupture. In the context of the earlier 2020 M7.6 Simeonof earthquake (Crowell & Melgar, 2020; Liu et al., 2021), the sea surface deformation in our model is largest in sections that did not rupture during that event, which can be seen in Figures 1 and 3. Some sections are observed to have overlapping rupture with the Simeonof source zone. We expect some uncertainty given the noisy input from the vertical deformation. The checkerboard test in Figures S6-8, shows smearing of the megathrust slip. Since

this is an inversion of the vertical pattern, itself obtained by inversion, we lack the ability to discern fine quality structures with it. Indeed, the misfits in Figure 3 show that the broad pattern of deformation is resolved but the short-wavelength details are not. From crustal deformation, we see that the hinge-line depicted by the inversion is very close to the rupture extent of Simeonof, which would suggest that the majority of the megathrust co-seismic slip occurred on the part of the interface that did not rupture previously. This point is further supported by the distributions of slip from the three megathrust earthquakes in this section of the Alaskan Subduction Zone as can be seen from Figure 3. The slip on the strike-slip fault is significantly different from that imaged by the USGS model; however, the checkerboard in Figure S8 shows very low resolution (<0.2) everywhere on the strike-slip geometry. This is unsurprising since we are only using vertical deformation which is easily overprinted by the megathrust-induced deformation.

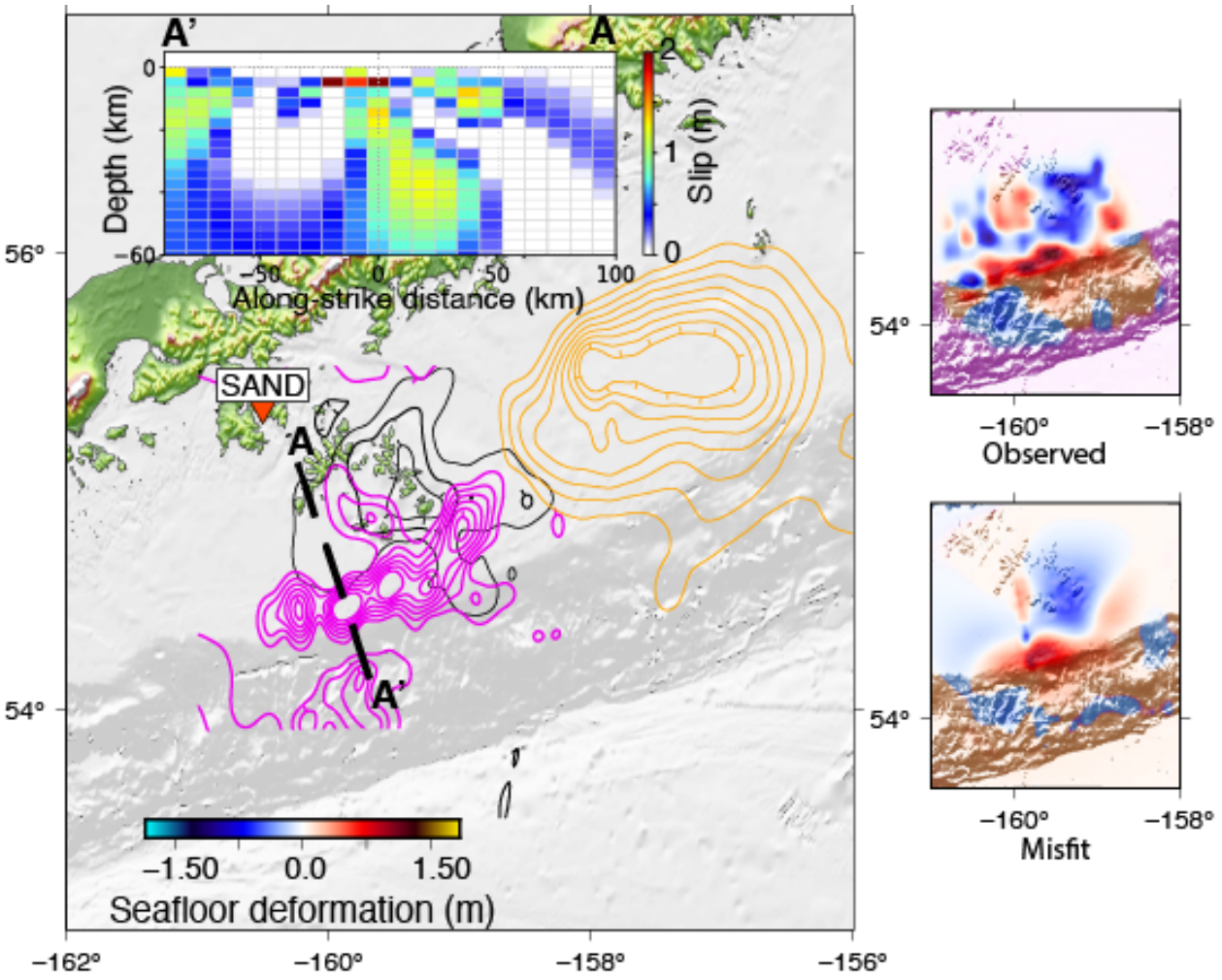

Figure 3. *Proposed earthquake source for the 2020 Sand Point tsunami. The magenta contours show the megathrust co-seismic slip for the October event. Contour spacing every 0.5m from 0m to 3m. The black for the July 2020 event. The orange for the July 2021 event. We show a cross-section of co-seismic slip for the strike-slip component of the October 2020 event denoted by the dotted-black line. The max slip contour is 3m.*

So, while the exact details of the slip that potentially produces the Sand Point tsunami are difficult to pin down exactly with this method, there is a strong case to be made that megathrust slip is a good explanation for it. Here lies a conundrum. In the joint inversion of Figure 3 the magnitude of the slip for both the strike-slip and megathrust amounts to Mw 8.00 ($M_o = 1.28\text{x}10^{21}$N-m). This implies that large amounts of megathrust slip went undetected by seismic data but are required by water-level inversion. We cannot at present resolve

the issue of how such a large quantity of slip would go "undetected" by far field seismic data. We posit that the megathrust slip ruptures in such a way that it was devoid or at least very depleted in seismic radiation. Coupled with the strike-slip seismic radiation happening concurrently, the megathrust component of the event could have been masked by the strike-slip component.

It has been noted that near-trench "tsunami earthquakes" rupturing through low rigidity portions of the megathrust can have this feature (e.g. Satake & Tanioka, 1999) and are depleted of both far-field (Newman et al., 2012) and near-field (Sahakian et al., 2020) seismic radiation. A characteristic of these is very slow rupture (e.g., Riquelme & Fuentes, 2021). To test for this, we modified the water level inversion to be time-dependent, we delayed each of the Gaussian unit sources assuming four very slow rupture velocities (0.25, 0.5, 1.0, and 1.5 km/s, Figures S9-43) radiating from the USGS hypocenter (54.602°N 159.626°W). We find that the slow ruptures degrade the fits to the tide gauges, most notably at Sand Point. The first arrivals for the most part are similar; however, the later arrivals no longer fit the observed data as well as the instantaneous model. The resulting slip patterns have less trench-ward slip at the slower rupture speeds and more at the faster rupture speeds. The slower rupture speeds have less slip of 3m and more than do the faster rupture speeds. Overall, we find that the slow ruptures are rougher with more slip in excess of 3m. Tsunami data have very limited sensitivity to rupture speed (e.g. Williamson et al., 2019) but the degradation of the fits suggests this is not a good model. Another possibility discussed by Ma & Nie (2019) is that the rupture progresses at a more "traditional" speed, since most of the slip occurs at ~15 km depth, but that rise-time is very long (and slip-rates are very low). This would make sense since most of the Shumagin segment is imaged to be mostly creeping and thus can reasonably be inferred to prefer rate-strengthening modes of rupture. Indeed (Crowell & Melgar, 2020), imaged some afterslip in this portion of the megathrust. In this model the megathrust slip during the Sand Point earthquake would be a peculiar kind of "fast" slow-slip. The rupture front propagates at a traditional speed, near shear-wave speeds, but once slip starts it is very slow. These processes would ostensibly be enough to keep the true extent of the megathrust co-seismic slip 'silent' in the seismic data. Moreover, the Mw 8.6 1946 earthquake on the neighboring Sanak segment was highly deficient in seismic radiation, with a teleseismic magnitude of only 7.4, indicating there may be some structural control on the megathrust that generates slow and long ruptures devoid of seismic radiation (Lopez & Okal, 2006).

Future work to elucidate this perplexing behavior should include a systematic exploration of the parameters needed to recreate all geophysical observables with a unified kinematic rupture model. There is regional strong motion and high-rate GNSS data that can be brought to bear. The issue is tricky since inversion for rupture onset times and rise-times, in addition to slip, is highly non-linear. But it is possible with linearized inversion techniques to explore complex ruptures such as this (e.g., Goldberg et al., 2020). The water level data at both the tide gauges and the DART buoys can be used as a constraint

or boundary condition that must be satisfied for such models to be deemed plausible.

4. Conclusion

We have shown that strike slip models for the 2020 Sand Point earthquake event are inadequate for generating the observed tsunami. Using water-level inversion techniques and vertical offset inversions we find that there was potentially co-seismic slip along the megathrust during the October 19, 2020 Sand Point strike-slip earthquake. The sea surface deformation necessary to recreate the tsunami waveforms at the Alaskan and Hawaiian tide gauges as well as the DART buoys requires it. Slip on both the strike-slip fault and the megathrust is equivalent to a Mw 8.00. We find that a slow rupture propagation speed does not explain the observations well so we posit that the megathrust slip does not contribute much seismic radiation perhaps due to slow slip rates during rupture. In this model the megathrust slip is "fast" slow-slip. The rupture front propagates at traditional near shear-wave speeds across the fault but produces very slow slip-rates.

Data Availability Statement

The water level data for the DART buoys can be obtained from the DART website (https://www.ndbc.noaa.gov/dart.shtml), for the tide gauges it can be obtained from NOAA's CO-OP the Environmental Research Division's Data Access Program (ERDDAP) server (https://opendap.co-ops.nos.noaa.gov/erddap/index.html), the vertical offset for AC12 was obtained from the Nevada Geodetic Laboratory website (http://geodesy.unr.edu/PlugNPlayPortal.php). The water level inversion code is available from Github (https://github.com/ssantellanes/water-level-inversion) and archived on Zenodo at Santellanes et al. (2021). The static slip inversions were generated using the FakeQuakes code which is part of the MudPy source modeling toolkit available on GitHub (https://github.com/dmelgarm/MudPy), the latest version is archived on Zenodo at Melgar (2021).

Acknowledgments

We'd like to thank Rich Briggs and Rob Witter for their discussion of Alaskan earthquakes. This work was partially funded by NASA grants # 80NSSC19K0360 and 80NSSC19K1104.

References

Abers, G. A. (1992). Relationship between shallow- and intermediate-depth seismicity in the Eastern Aleutian Subduction Zone. *Geophysical Research Letters*, *19*(20), 2019–2022. Retrieved from https://doi.org/10.1029/92GL02060

Bécel, A., Shillington, D. J., Delescluse, M., Nedimović, M. R., Abers, G. A., Saffer, D. M., et al. (2017). Tsunamigenic structures in a creeping section of the Alaska subduction zone. *Nature Geoscience*, *10*(8), 609–613. https://doi.org/10.1038/NGEO2990

Blewitt, G., W. C. Hammond, and C. Kreemer (2018), Harnessing the GPS data explosion for interdisciplinary science, Eos, 99, https://doi.org/10.1029/2018EO104623

Crowell, B. W., & Melgar, D. (2020). Slipping the Shumagin Gap: A Kinematic Coseismic and Early Afterslip Model of the Mw 7.8 Simeonof Island, Alaska, Earthquake. *Geophysical Research Letters*, *47*(19), 1–7. https://doi.org/10.1029/2020GL090308

Davies, J., Sykes, L., House, L., & Jacob, K. (1981). Shumagin Seismic Gap, Alaska Peninsula: History of Great Earthquakes, Tectonic Setting, and Evidence for High Seismic Potential. *Journal of Geophysical Research*, *86*, 3821–3855.

Elbanna, A., Abdelmeguid, M., Ma, X., Amlani, F., Bhat, H. S., Synolakis, C., & Rosakis, A. J. (2021). Anatomy of strike-slip fault tsunami genesis. *Proceedings of the National Academy of Sciences*, *118*(19).

Fukao, Y. (1979). Tsunami earthquakes and subduction processes near deep-sea trenches. *Journal of Geophysical Research: Solid Earth*, *84*(B5), 2303–2314. https://doi.org/10.1029/JB084iB05p02303

Goldberg, D. E., Melgar, D., Sahakian, V. J., Thomas, A. M., Xu, X., Crowell, B. W., & Geng, J. (2020). Complex rupture of an immature fault zone: A simultaneous kinematic model of the 2019 Ridgecrest, CA earthquakes. Geophysical Research Letters, 47(3), e2019GL086382.

Hayes, G. P. (2017). The finite, kinematic rupture properties of great-sized earthquakes since 1990. *Earth and Planetary Science Letters*, *468*, 94-100.

Herman, M. W., & Furlong, K. P. (2021). Triggering an unexpected earthquake in an uncoupled subduction zone. *Science Advances*, *7*(13), 1–10. https://doi.org/10.1126/sciadv.abf7590

Kanamori, H., & Kikuchi, M. (1993). the 1992 Nicaragua Earthquake. *Nature*, *361*(February), 714–716.

Larson, K. M., Lay, T., Yamazaki, Y., Cheung, K. F., Ye, L., Williams, S. D. P., & Davis, J. L. (2020). Dynamic Sea Level Variation from GNSS: 2020 Shumagin Earthquake Tsunami Resonance and Hurricane Laura. *Geophysical Research Letters*. https://doi.org/10.1029/2020gl091378

Lay, T., Kanamori, H., Ammon, C. J., Koper, K. D., Hutko, A. R., Ye, L., et al. (2012). Depth-varying rupture properties of subduction zone megathrust faults. *Journal of Geophysical Research: Solid Earth*, *117*(4), 1–21. https://doi.org/10.1029/2011JB009133

LeVeque, R. J., George, D. L., & Berger, M. J. (2011). Tsunami modelling with adaptively refined finite volume methods. *Acta Numerica*, *20*, 211-289.

Li, S., & Freymueller, J. T. (2018). Spatial Variation of Slip Behavior Beneath the Alaska Peninsula Along Alaska-Aleutian Subduction Zone. *Geophysical Research Letters*, *45*(8), 3453–3460. https://doi.org/10.1002/2017GL076761

Lin, J. T., Aslam, K. S., Thomas, A. M., & Melgar, D. (2020). Overlapping regions of coseismic and transient slow slip on the Hawaiian décollement. *Earth and Planetary Science Letters*, *544*, 116353. https://doi.org/10.1016/j.epsl.2020.116353

Liu, C., Lay, T., Xiong, X., & Wen, Y. (2020). Rupture of the 2020 MW 7.8 Earthquake in the Shumagin Gap Inferred From Seismic and Geodetic Observations. *Geophysical Research Letters*, *47*(22), 1–9. https://doi.org/10.1029/2020GL090806

Ma, S., & Nie, S. (2019). Dynamic wedge failure and along-arc variations of tsunamigenesis in the Japan trench margin. Geophysical Research Letters, 46(15), 8782-8790.

Melgar, D., & Bock, Y. (2013). Near-field tsunami models with rapid earthquake source inversions from land- and ocean-based observations: The potential for forecast and warning. *Journal of Geophysical Research: Solid Earth*, *118*(11), 5939–5955. https://doi.org/10.1002/2013JB010506

Melgar, D., & Bock, Y. (2015). Kinematic earthquake source inversion and tsunami runup prediction with regional geophysical data. *Journal of Geophysical Research: Solid Earth*, 120(5), 3324-3349.

Melgar, D., LeVeque, R. J., Dreger, D. S., & Allen, R. M. (2016). Kinematic rupture scenarios and synthetic displacement data: An example application to the Cascadia subduction zone. *Journal of Geophysical Research: Solid Earth*, *121*(9), 6658-6674.

Melgar, D. (2021). dmelgarm/MudPy: v1.3. Zenodo. doi:10.5281/zenodo.5397091

Okal, E. A., & Synolakis, C. E. (2003). A theoretical comparison of tsunamis from dislocations and landslides. *Pure and Applied Geophysics*, *160*(10–11), 2177–2188. https://doi.org/10.1007/s00024-003-2425-x

Riquelme, S., & Fuentes, M. (2021). Tsunami Efficiency Due to Very Slow Earthquakes. *Seismological Research Letters*. https://doi.org/10.1785/0220200198

Sahakian, V. J., Melgar, D., & Muzli, M. (2019). Weak near-field behavior of a tsunami earthquake: Toward real-time identification for local warning. Geophysical Research Letters, 46(16), 9519-9528.

Santellanes, S.R., Lin, J.T., & Melgar, D.. (2021, September 9). ssantellanes/water-level-inversion: First release (Version v1.0.0). Zenodo. https://doi.org/10.5281/zenodo.5498175

Satake, K., & Tanioka, Y. (1999). Sources of Tsunami and Tsunamigenic Earthquakes in Subduction Zones. *Pure and Applied Geophysics*, *154*, 467–483. https://doi.org/10.1007/978-3-0348-8679-6_5

Titov, V. V., González, F. I., Bernard, E. N., Eble, M. C., Mofjeld, H. O., Newman, J. C., & Venturato, A. J. (2005). Real-time tsunami forecasting: Challenges and solutions. *Natural Hazards*, *35*(1), 41–58. https://doi.org/10.1007/s11069-004-2403-3

Tsai, V. C., Ampuero, J. P., Kanamori, H., & Stevenson, D. J. (2013). Estimating the effect of Earth elasticity and variable water density on tsunami speeds. Geophysical Research Letters, 40(3), 492-496.

Tsushima, H., Hino, R., Fujimoto, H., Tanioka, Y., & Imamura, F. (2009). Near-field tsunami forecasting from cabled ocean bottom pressure data. *Journal of Geophysical Research: Solid Earth*, *114*(6), 1–20. https://doi.org/10.1029/2008JB005988

Williamson, A., Melgar, D., & Rim, D. (2019). The effect of earthquake kinematics on tsunami propagation. Journal of Geophysical Research: Solid Earth, 124(11), 11639-11650.

Witter, R. C., Briggs, R. W., Engelhart, S. E., Gelfenbaum, G., Koehler, R. D., and Barnhart, W. D. (2014), Little late Holocene strain accumulation and release on the Aleutian megathrust below the Shumagin Islands, Alaska, *Geophysical Research Letters*, 41, 2359– 2367, doi:10.1002/2014GL059393.

Ye, L., Lay, T., Kanamori, H., & Rivera, L. (2016). Rupture characteristics of major and great (Mw 7.0) megathrust earthquakes from 1990 to 2015: 1. Source parameter scaling relationships. *Journal of Geophysical Research: Solid Earth*, *121*(2), 826-844.

Yue H., Lay T., Li L., Yamazaki Y., Cheung K.F., Rivera L., Hill E.M., Sieh K., Kongko W., & Muhari, A. Validation of linearity assumptions for using tsunami waveforms in joint inversion of kinematic rupture models: Application to the 2010 Mentawai Mw 7.8 tsunami earthquake. *Journal of Geophysical Research: Solid Earth*. 2015,120(3),1728-47.